Mineralogical Magazine, June 2016, Vol. 80(4), pp. 567–584

Reaction aureoles around uraninites within biotite and plagioclase: evidence of low-temperature sequential fluid alteration and *LREE*-mobilization from monazite

MANOJ K. OZHA[1], BISWAJIT MISHRA[1,*] AND AIVELIAGARAM V. JEYAGOPAL[2]

[1] Department of Geology and Geophysics, Indian Institute of Technology, Kharagpur 721302, India
[2] Atomic Minerals Directorate for Exploration and Research, Shillong 793019, India

[*Received 16 April 2015; Accepted 17 November 2015; Associate Editor: Giancarlo Della Ventura*]

ABSTRACT

Optical microscopy, Raman spectroscopy and electron probe microanalyses were conducted on a migmatitic metapelite to investigate the effects of alpha radiation and subsequent alteration at the interface between uraninite inclusions and the host minerals biotite, chlorite and albitic plagioclase. The study reveals (1) anomalous colouration under the polarizing microscope; (2) pertinent changes in the characteristic Raman spectra of host phases; (3) reaction aureoles, composed of secondary phases (*viz.* chlorite and K-feldspar) of various sizes (~15–45 μm) within biotite and plagioclase, respectively; (iv) K-feldspatization and sericitization of plagioclase at the grain boundaries; (5) agreement between the observed α-penetration depths and the Monte-Carlo simulation results; and (6) dissolution textures within the matrix monazites. Analysis of the compositions of the reaction aureoles in albitic plagioclase reveals a systematic distribution of K-feldspar-, *LREE*- and clay-rich zones; while the same in biotite is composed of secondary chlorite.

The growth sequence of the secondary phases indicates an influx of a K-rich fluid, following intense radiation damage, efficiently superimposed by *LREE*-metasomatism and later acidic alteration. These changes took place under low-temperature (≤150°C) conditions, wherein radial cracks (within plagioclase) and cleavages/fractures (within biotite) favoured fluid infiltration-circulation into the reaction aureoles. Depletion of the *LREE*s from the dissolved matrix monazites and their enrichment as a discrete *LREE* phase within the damaged aureoles in plagioclase demonstrate micrometre-scale *LREE* mobility.

KEYWORDS: uraninite, radiation halo, K-metasomatism, *LREE* mobilization.

Introduction

THE effect of radiation on minerals in the vicinity of radioactive U-Th-bearing grains has been known for more than a century (Joly, 1907), and investigations into the factors responsible have increased over the past two decades, mainly due to our improved understanding of the crystal structure and its distortion in the radioactive mineral and adjacent phases (Ewing *et al*., 2003; Seydoux-Guillaume *et al*., 2009). The alpha (α) decay of U-Th, stimulates structural adjustments in the original crystal structures of the host and the neighbouring minerals, which eventually produces concentric rings of structural distortions in the surrounding mineral centring the radioactive grain (Ewing, 1994). These rings are termed as 'pleochroic halos' or 'radiohalos', which are easily identified under the petrological microscope and thereby can be used as a tool to identify radioactive minerals in thin sections.

With the use of Raman spectroscopy, electron probe microanalyses (EPMA), and transmission electron microscopy, the scope of radiation damage studies in geosciences have gained momentum. Such studies mainly include (1) irradiation effects on the associated phases (Nasdala *et al.*, 2001, 2006); (2) durability of ceramics that could be used

E-mail: bmgg@iitkgp.ac.in
DOI: 10.1180/minmag.2016.080.062

© 2016 The Mineralogical Society

in nuclear-waste forms (Weber *et al.*, 1998); and (3) impact of irradiation on the U-Th-Pb systematics of radioactive minerals used for dating (e.g. Ewing *et al.*, 2003).

The earliest documentation of radiohalos was by Joly (1907). Later published works focused on the reasons behind the formation of radiohalos, which is a consequence of the α-decay series of ^{238}U, ^{235}U, and ^{232}Th, liberated by the associated radioactive mineral inclusions (Gentry, 1973, 1974; Pal, 2004). Raman studies have demonstrated α-particle-induced metamictization in biotite (Nasdala *et al.*, 2001), chlorite and cordierite (Nasdala *et al.*, 2006) in the vicinity of radioactive grains. In addition, there are also several studies on metamictization of radioactive minerals (see Ewing *et al.*, 2000), such as zircon (Ewing *et al.*, 2003), allanite (Janeczek and Eby, 1993), and thorite (Farges and Calas, 1991).

Halos of secondary phases (calcite, pyrite, goethite and various U-Th-*REE*-bearing minerals) at the interface between uraninite/uranothorite grains within host biotite and chlorite were reported by Rimsaite (1982), from granites associated with uranium deposits in the Grenville province, Canada. Recent studies of secondary phases at the radioactive host-inclusion interfaces include those in diopside and calcite (Seydoux-Guillaume *et al.*, 2009), and in quartz, albite, K-feldspar, and cordierite (Prochazka *et al.*, 2011). These studies demonstrate that long-time α-radiation-induced intense destruction of the host mineral structure will create a potential site for alteration. Similarly, radiation damage in monazites during a low-temperature hydrothermal event can facilitate alteration and thereby mobilize dissolved elements (Seydoux-Guillaume *et al.*, 2012).

This investigation integrates optical microscopy, Raman spectroscopy, Monte-Carlo simulation, and EPMA to address the irradiation effect in host phases (biotite, chlorite, and plagioclase) surrounding uraninite inclusions. Another focus is on post-irradiation fluid-assisted alteration of the non-radioactive host phases surrounding uraninite grains, and also the chemical evolution associated with the *LREE* mobilization from monazite.

Sample description and petrography

The sample comes from the Potla Formation of the Mangalwar Complex that forms the migmatitic basement (Heron, 1953; Gupta *et al.*, 1997; Fig. 1*a*) within the Aravalli-Delhi Fold Belt in north-western India. The sample was collected from a borehole (SMK-5, 127 m depth; 25°12′ 38.2″N, 74°27′16.8″E) located on the eastern limb of the Samarkiya antiform (Fig. 1*b*). Based on EPMA radiometric age determination of monazites, three ages of amphibolite-facies metamorphism have been assigned at ∼1.82 Ga, ∼1.33 Ga, and ∼0.98 Ga for the metapelites in and around the Samarkiya area (Ozha *et al.*, 2016). In addition, the oldest and the youngest ages were reported earlier from the rocks of the Mangalwar Complex exposed around Bhinai (∼120 km north-west of the present study area, Fig. 1*a*) (Buick *et al.*, 2006, 2010; Bhowmik *et al.*, 2010).

The sample studied is a migmatitic metapelite containing quartz, biotite, chlorite, albitic plagioclase, rare K-feldspar and muscovite/sericite. Accessory phases include uraninite, apatite, monazite, zircon, xenotime and pyrite. Numerous radiohalos surrounding uraninite and zircon can be seen in thin section (Figs 2*a*,*b*). The pervasive foliation of the rock is defined by biotite (Fig. 2*a*). Although, albitic plagioclases in the sample are found to be fresh, some altered reaction fronts develop at the grain boundaries (e.g. Fig. 2*c*). K-feldspars and muscovite/sericite in the sample are very rare, and are restricted to the proximity of the altered domains. Euhedral-to-subhedral uraninite (UO_2) grains of various sizes (∼2–25 μm) occur within and along the grain boundaries of biotite, chlorite, and plagioclase (e.g. Fig. 2*d*). All mineral abbreviations, used in the text are after Whitney and Evans (2010).

Experimental techniques

In the present study, the biotite, chlorite and plagioclase hosts containing uraninite (UO_2) were considered for characterization of the radiation damage. Radio-centres with varying sizes (∼2–23 μm) occurring on the surface of these minerals were studied. Images of radiohalos were captured and measurements of the halo and inclusion diameters were performed using *LEICA-QWIN* image analysing software, where a mean of 4–5 radii measurements were considered for each individual ring. This was followed by micro-Raman analysis of selected radiohalos and subsequent back-scattered electron (BSE) and X-ray element imaging and EPMA. The rationale behind this sequence is to avoid bias in Raman results, which usually occurs if EPMA is performed prior to Raman spectroscopy (cf. Nasdala *et al.*, 2006). All the micro-beam studies were carried out in the

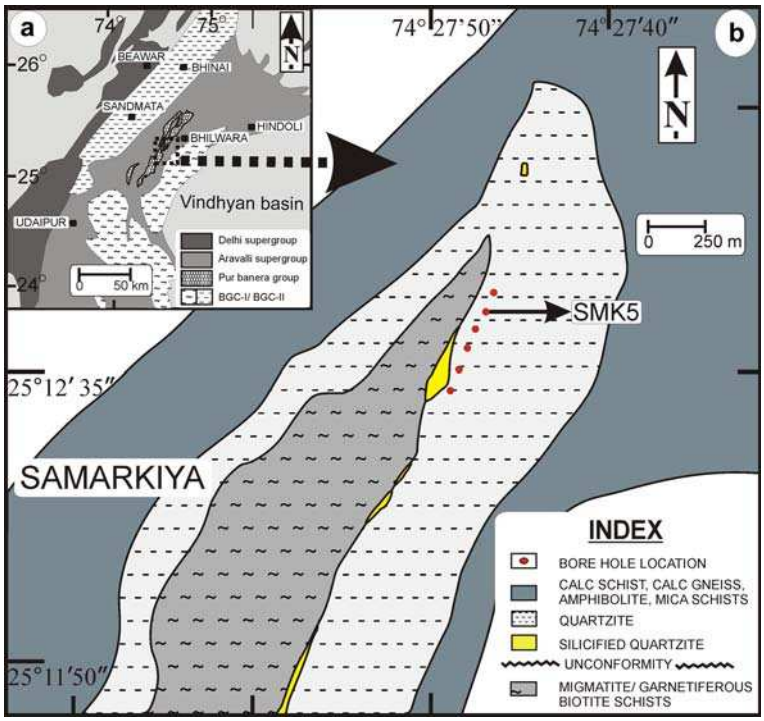


FIG. 1. (*a*) Regional geological map of the Aravalli Delhi Fold Belt, showing the distribution of different lithological units (modified after Heron, 1953; Gupta *et al.*, 1997). (*b*) Geological map of the Samarkiya area (modified after the Atomic Minerals Directorate for Exploration and Research, AMDER), showing the location of the boreholes. The samples for this study belong to borehole #SMK–5.

Department of Geology and Geophysics, at the Indian Institute of Technology, Kharagpur.

Raman spectra were obtained using a RENISHAW-RM1000B Laser Raman Micro-spectrometer (LRM), attached to a Leica DMRL microscope with a motorized X-Y stage. The system is equipped with an edge filter to block the Rayleigh lines. It has a confocal configuration with a thermoelectrically cooled CCD detector, air-cooled laser, and software to acquire and evaluate the spectral data. A 50× microscope objective was used. Irradiation was performed by using 1% of a 300 mW 785 nm NIR diode laser, for an acquisition time of 20 s. Routine calibration of the instrument is performed using a Si standard that gives the first order Raman band at 520 ± 1 cm^{-1}. Raman spectra were acquired with a lateral resolution of <5 μm and estimated depth resolution of ≤2 μm.

Back-scatter electron and X-ray element imaging and mineral analyses were performed with 4-WDS CAMECA SX-100 EPMA. Major-element analyses were carried out with a beam current regulated at 20 nA and acceleration voltage of 15 kV, whereas trace elements were analysed with a beam current of 40 nA (for uraninite and the *LREE* phase) and 200 nA (monazite) and acceleration voltage of 20 kV. The beam size was 1 μm for all analyses. A detailed protocol of major-element analysis for silicates is given in Hazarika *et al.* (2015). For trace-element analysis of uraninite, monazite, and the *LREE* phase both natural and synthetic standards were used. The specific standards used for calibration were: pyromorphite for Pb; UO_2 for U; ThO_2 for Th; synthetic glass containing *REE*s for La, Ce, Nd, Pr, Sm, Ho, Dy, Gd; apatite for Ca and P; yttrium aluminium garnet (YAG) for Y; hematite for Fe; corundum for Al and Th-glass for Si. For Pb analysis the *M*α line was chosen with a peak count time of 300 s and background count time of 150 s on both sides. The U-*M*β line was used for U to avoid interference of U-*M*α with Th-*M*β. Counting times for U*M*β and Th-*M*β lines were set at 200 s for peak and 100 s for background

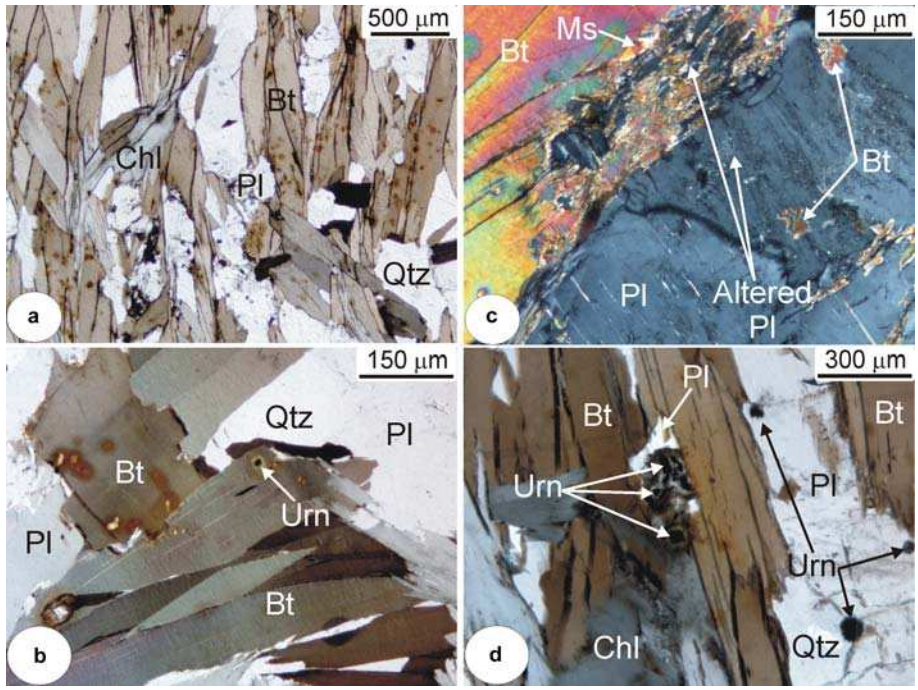


FIG. 2. Representative transmitted-light photomicrographs showing the textural relations and types of radiohalos in the sample: biotite defines the fabric (*a*); anomalous colouration in biotite surrounding uraninites (*b*); crossed-polar view of plagioclase showing alteration at the grain boundary (*c*); uraninite grains within and at the boundaries of host minerals (*d*). Mineral abbreviations are after Whitney and Evans (2010). See text for details.

on both sides. Lines used for the *REE*s were: *L*α for La, *L*α for Ce; *L*α for Nd; *L*β for Pr; *L*α for Sm; *L*β for Ho; *L*α for Dy and *L*β for Gd. The spectral interferences of the Y-*L*γ_2, Y-*L*γ_3 lines of yttrium on Pb-*M*α line of Pb and Th-*M*γ, Th-M_3N_4 of Th on U-*M*β of U were corrected during calibration using the *Peak Sight* Software of CAMECA SX-100. The raw EPMA data were matrix corrected with the *PAP* correction program by Pouchou and Pichoir (1984).

Results

Halo characterization

The sample contains numerous halos within biotite and chlorite, which surround radio-centres like zircon, monazite and uraninite. In contrast, radiohalos within plagioclase are restricted to uraninite grains. These halos are associated largely with more than one concentric ring in biotite and chlorite (e.g. Figs 2*a*, *b*), where the radiohalo size varies linearly with that of the radio-centre, i.e. the uraninite grain (Fig. 3). A brief description of the changes within these radiation damaged areas is provided below.

Under transmitted light, the interface of large (≥10 μm) uraninite grains within the biotite and chlorite host are characterized by an encircled zone (~15 μm) of intense anomalous colouration (Figs 4*a*, *b*). In contrast, the same feature within albitic plagioclase has a ~45 μm circle of three distinct coloured zones (I, II and III; Fig. 4*c*), where the light cocoa-brown coloured region represents zone-I, surrounded discontinuously by a nearly circular reddish-brown region (zone-II). These two zones are further rimmed by a darker, porous cryptocrystalline aggregate (zone-III). Thus, the observed optical features indicate a higher degree of metamictization in the above minerals at the interface of uraninite grains. For assessing the radiation damage, Raman studies were attempted in and around the radiohalos. The Raman spectra of biotite and chlorite, surrounding the uraninite grains exhibit a continuous decrease in the intensities of characteristic Raman bands and a continuous increase in their peak widths at half

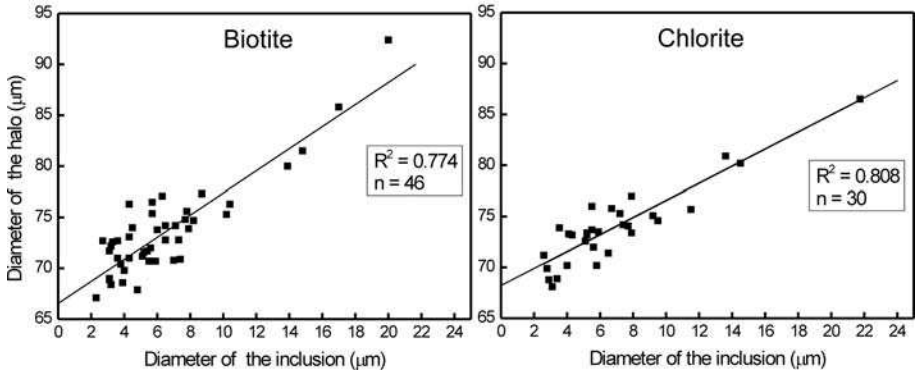


FIG. 3. Plots showing the linear correlation between the size of the uraninite grains and their surrounding halo diameters within biotite and chlorite.

height, towards the radio-centre (Figs 4*d*, *e*). Most importantly, the obtained Raman spectrum at a distance of ~5 μm away from the uraninite inclusion in biotite (Fig. 4*d*) appears similar to that of damaged chlorite (Fig. 4*e*), implying alteration of biotite to chlorite following structural damage. Similarly, presumably sodic plagioclase at the interface of uraninite yielded a Raman spectrum of K-feldspar (Figs 4*c*, *f*). Back-scatter electron images of the damaged area surrounding uraninites in different minerals also show significant compositional changes (Fig. 5). The circular zone (~15 μm) close to the interface with uraninite in biotite appears darker when compared to its pristine counterpart (Fig. 5*b*). Similarly, the damaged region in plagioclase is represented by a ~45 μm wide area with three discrete zones (I, II, and III; Fig. 5*c*). Zone-I appears light grey, while a patchy brighter part with numerous fibrous phases represents zone-II. Zone-III corresponds to the darkest region within the radiation-damaged area, which roughly encircles the other two zones. On the contrary, chlorite retains its homogeneity within and outside the halo area (Fig. 5*d*). The form of the aureoles invariably mimics the shape of the radioactive mineral inclusion. Note that only halos surrounding uraninite grains with sizes ≥10 μm will be considered further in this study.

Textural properties of the reaction zones

Reaction zones/aureoles in the sample are present both within and at the boundaries between the host minerals and its radioactive inclusions (Fig. 5*a*). The aureoles within biotite are found to be connected with cleavages and fractures (e.g. Fig. 5*b*), and filled with chlorite-bearing microveins (Fig. 5*e*). The aureoles within plagioclase are associated with radial cracks, which further extend to the grain boundaries of the host mineral (Fig. 5*f*). Uraninite grains occurring at the boundary of mineral phases are enclosed by diverse sectors of reaction zones, where an individual sector constitutes different minerals (Fig. 5*g*). Occasionally, plagioclases are found to be permeated by biotite flakes (e.g. Fig. 5*h*) and connected by altered K-feldspar (e.g. Fig. 5*f*). Pyrite and zircon grains have also been observed to be associated with the damaged aureoles in plagioclase (Figs 5*g*, *i*).

Mineral chemistry: primary and secondary phases

Representative EPMA results of selected primary and secondary minerals are given in Table 1. The data show homogeneous compositions of matrix biotite and chlorite. Considering all Fe to be bivalent and based on 24 and 18 oxygen atoms per formula unit (apfu), the representative calculated chemical formulae for biotite and chlorite are $[(K_{1.76}Na_{0.05})(Mg_{2.99}Fe_{1.98}Al^{vi}_{2.53}Ti_{0.13})(Al^{iv}_{0.46}Si_{5.47}O_{20})(OH)_4]$ and $[(Fe_{2.27}Mg_{3.59}Al^{vi}_{0.46})(Si_{3.47}Al^{iv}_{2.98}O_{10})(OH)_8]$, respectively and can be classified broadly as phlogopite and clinochlore. Calculated average chemical formula of the unaltered matrix plagioclase, based on 8 oxygen apfu, is $[(Na_{1.62}Ca_{0.28})(Al_{1.18}Si_{2.57})O_8]$, with $X_{An} \approx 0.15$, whereas the altered parts show a significant content of K ($X_{Kfs} \approx 0.14$; analysis 4: Table 1). The phase in zone-I within the plagioclase aureoles (Fig. 5*c*) retains a composition close to K-feldspar (analysis 11: Table 1), while at the grain

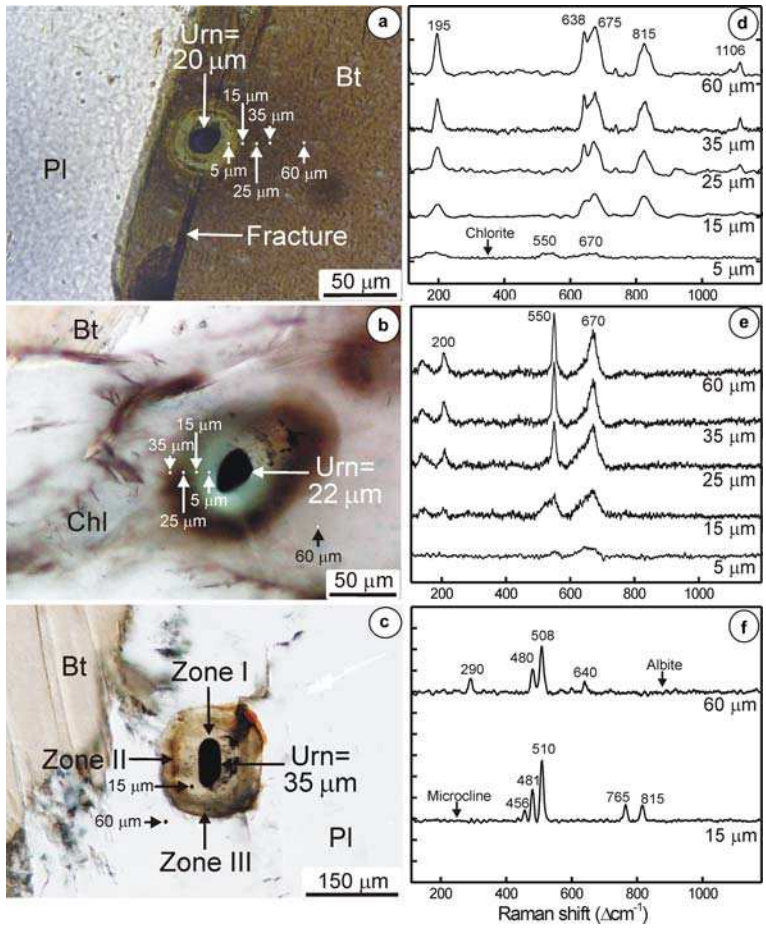


FIG. 4. Photomicrographs of representative radiohalos with intense colouration at the interface between large (≥10 μm) uraninite grains within biotite (*a*), chlorite (*b*), and plagioclase (*c*) hosts, and their corresponding Raman spectra (Ar^+785-nm excitation) (*d*–*f*). Measurements were made within the radiohalo at an interval of ~10 μm away from the uraninite inclusions and one in the adjacent unaffected area of the host at a distance of ~60 μm. Note the spectra in biotite (at ~5 μm, *d*) and plagioclase (at ~15 μm, *f*) resemble that of chlorite and microcline, respectively.

boundaries in the matrix it is found to be more Na-rich ($X_{Ab} = 0.30$; analysis 5: Table 1). The Muscovite/sericite composition in the sample remains homogeneous. Uraninites in the sample have inhomogeneous compositions, where the compositional variations are: UO_2 (77.64–81.23 wt.%), ThO_2 (4.27–5.28 wt.%), and PbO (12.54–16.35 wt.%) (analyses 13–14: Table 1).

The secondary phase occurring at the interface between large (≥10 μm) uraninite grains and host biotite is chlorite with a composition similar to that of matrix chlorite (analysis 8: Table 1). In contrast, the secondary phases within plagioclase are rather intricately distributed within three zones. Zone-I (Fig. 5*c*) has a K-feldspar composition (analysis 11: Table 1). The surrounding patchy and fibrous mineral (zone-II, Fig. 5*c*) represents a still unidentified *LREE* phase (*LREE*s ≈ 55 wt.% oxide; analyses 15–16: Table 1), which is subsequently enclosed by a clay mineral (zone-III, Fig. 5*c*). Due to high porosity, it was difficult to analyse the clay mineral. However, composition of the clay phase probably resembles that of illite and one representative analysis is presented in Table 1 (analysis 12). Chlorite preserves its chemical homogeneity at the uraninite interface (analysis 9: Table 1).

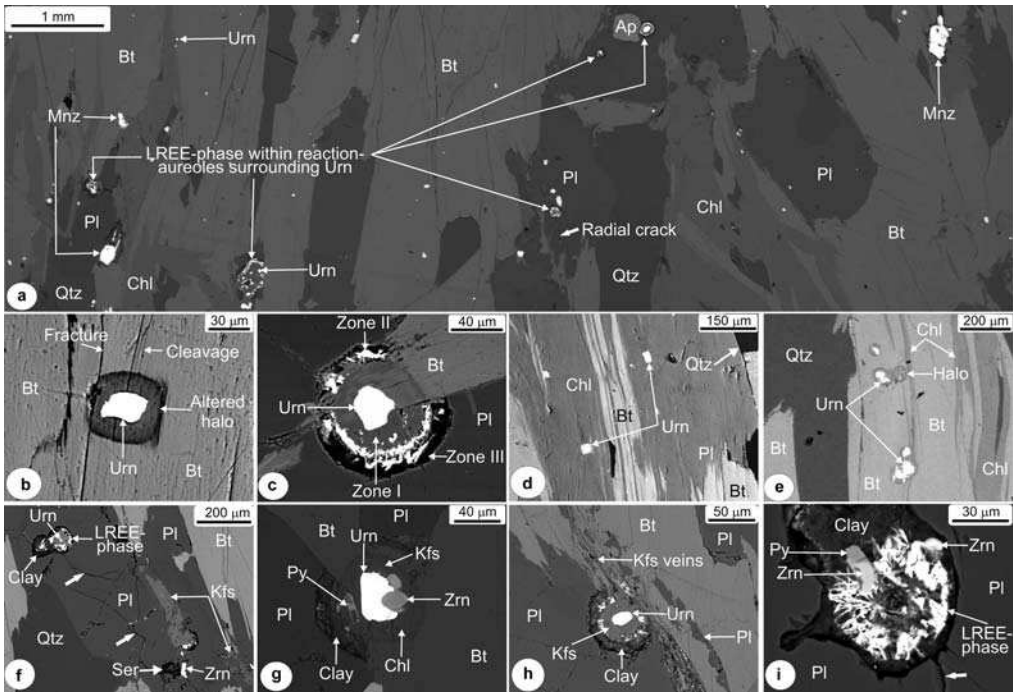


FIG. 5. Representative back-scattered electron (BSE) images with radiohalos surrounding uraninite grains in different minerals. A typical area from the thin section showing the occurrence of radiohalos and monazite (*a*); a halo at the interface between a large (≥10 μm) uraninite grain and host biotite containing one reaction rim (dark grey shade) (*b*); and three concentric rims (three zones) within plagioclase (*c*) were observed; while no such zones was observed within chlorite (*d*); growth of chlorite into the reaction rims through cleavages/fractures within biotite (*e*); radial cracks (shown by thick white arrows), K-feldspar connecting the reaction aureoles, and sericite within plagioclase (*f*); uraninite grain enclosed by different reaction sectors within biotite and plagioclase at the grain boundary (*g*); folia of biotite and K-feldspar veins connected to the halo (*h*); reaction rim associated with the *LREE*-bearing and the clay-mineral phase, pyrite, and zircon within plagioclase (*i*). See text for details.

Elemental systematics in reaction aureoles

For a better understanding of the element distributions within the reaction aureoles, X-ray element mapping of a representative reaction aureole (the domain in Fig. 5*c*) was carried out, as shown in Fig. 6. The reaction zone within adjacent biotite, displays a uniform increase of Al and Fe, whereas K was completely leached out. Spot analysis of the zone thus confirms post irradiation chloritization of biotite (analysis 8: Table 1) (e.g. Prochazka *et al.*, 2011). On the other hand, aureoles within plagioclase are characterized by a systematic distribution of elements. The interface between plagioclase and uraninite (zone-I) is composed entirely of an Al-K-rich phase, separated partly/entirely by a discontinuous low-Al/K and high-Ce phase (zone-II). Subsequently, the two zones are embayed by an intermediate-Al and K-depleted clay-mineral phase (zone-III) (analysis 12: Table 1). Additional insights into the element mobility through quantitative mass-balance calculations could not be performed for the alteration aureoles, because radiation halos were observed only in very small samples. However, the elemental distribution and the chemical variations most probably imply open system behaviour at thin-section scale.

SRIM/TRIM modelling

A full-quantum calculation based *SRIM/TRIM* (Stopping/Transfer and Range of Ions in Matter) software package (Ziegler *et al.*, 2006) was used to model the penetration depths of α particles into the radiohalos. The program involves Monte-Carlo simulation of the effect of the α decay penetration in a target mineral of known composition. The

TABLE 1. Representative compositions from electron probe microanalyses.

Textural domain	Matrix		Reaction domain at the grain boundary					Within radiohalo		Within plagioclase reaction aureole		
Anal. no.	1	2	3	4	5	6	7	8	9	10	11	12
Mineral	Bio	Chl	Pl	Pl_Alt	Kfs	Ser	Ms	Bt_H	Chl_H	Pl	Kfs	Clay
SiO_2	37.69	26.46	64.70	62.92	63.20	46.94	50.20	26.20	26.60	65.57	66.23	53.30
TiO_2	1.20	0.05	b.d.l	b.d.l	0.05	0.73	0.63	0.05	0.09	b.d.l	b.d.l	b.d.l
Al_2O_3	17.48	22.28	22.30	23.39	20.90	33.19	34.80	22.60	22.53	22.31	18.46	18.30
Cr_2O_3	0.05	0.01	b.d.l	0.01	b.d.l	0.01	0.04	0.03	0.03	0.05	0.02	b.d.l
FeO	16.31	20.70	0.02	0.45	0.67	1.35	1.30	21.60	21.79	b.d.l	0.06	0.51
MnO	0.14	0.13	0.01	0.02	0.01	b.d.l	b.d.l	0.26	0.16	b.d.l	0.02	0.05
MgO	13.80	18.38	b.d.l	0.51	0.42	1.51	1.57	18.00	18.01	0.02	b.d.l	4.58
CaO	0.06	0.05	3.51	2.35	0.72	0.04	0.01	0.02	0.02	3.32	b.d.l	1.68
Na_2O	0.18	0.01	10.20	8.76	4.05	0.57	0.50	b.d.l	b.d.l	9.51	0.06	0.12
K_2O	9.55	0.09	0.03	1.56	9.23	10.14	8.83	b.d.l	0.01	0.10	16.33	2.93
Total	96.5	88.1	101	100	99.2	94.65	97.9	88.7	89.2	100.9	101.2	81.6
Oxygen	24	18	8	8	8	24	24	18	18	8	8	
Si	5.47	3.47	2.57	2.52	2.53	6.29	6.97	3.43	3.43	2.86	2.61	
Ti	0.13	b.d.l	1.18	1.25	1.11	0.07	0.07	b.d.l	0.01	1.15	0.97	
Al	2.99	3.44	b.d.l	b.d.l	b.d.l	5.24	5.70	3.48	3.42	b.d.l	b.d.l	
Cr	0.01	b.d.l	b.d.l	b.d.l	b.d.l	0.00	0.00	b.d.l	b.d.l	b.d.l	b.d.l	
Fe^{2+}	1.98	2.27	b.d.l	0.04	0.05	0.15	0.05	2.36	2.35	b.d.l	b.d.l	
Mn	0.02	0.01	b.d.l	b.d.l	b.d.l	b.d.l	b.d.l	0.03	0.02	b.d.l	b.d.l	
Mg	2.99	3.59	b.d.l	0.04	0.03	0.30	0.33	3.52	3.46	b.d.l	b.d.l	
Ca	0.01	0.01	0.28	0.19	0.06	0.01	b.d.l	b.d.l	b.d.l	0.16	b.d.l	
Na	0.05	b.d.l	1.62	1.40	0.65	0.15	0.14	b.d.l	b.d.l	0.80	0.01	
K	1.77	0.01	b.d.l	0.25	1.48	1.73	1.56	b.d.l	b.d.l	0.01	2.57	
X_{An}			0.150	0.100	0.030					0.160	0.000	
X_{Ab}			0.850	0.760	0.300					0.820	0.000	
X_{Or}			0.000	0.140	0.680					0.010	1.000	

Mineral abbreviations are after Whitney and Evans (2010); Alt: Altered; H: halo; b.d.l: below detection limit, other elements below detection limits are not shown.

energy involved in a single α decay produces photons, comprising a fast α particle (^{4}He nucleus), and a slow, heavy daughter recoil nucleus (Seydoux-Guillaume *et al.*, 2009). In the present study, the uraninites contain appreciable amounts of Th (analyses 13–14: Table 1) and thereby, preserve three major radio nuclides, i.e. ^{238}U, ^{235}U and ^{232}Th and consequently, it will produce 21 different α energies (see Table 2, Seydoux-Guillaume *et al.*, 2009). Monte-Carlo calculations were performed for each α energy, which irradiates perpendicularly onto the target minerals such as phlogopite [$(K_{1.76}Na_{0.05})(Mg_{2.99}Fe_{1.98}Al^{vi}_{2.53}Ti_{0.13})(Al^{iv}_{0.46}Si_{5.47}O_{20})(OH)_4$], clinochlore [$(Fe_{2.27}Mg_{3.59}Al^{vi}_{0.46})(Si_{3.47}Al^{iv}_{2.98}O_{10})(OH)_8$], and albitic plagioclase [$(Na_{0.87}Ca_{0.05})(Al_{1.05}Si_{2.97})O_8$], with *SRIM*-derived respective densities of ρ = 3.1, 2.65 and 2.61 g/cm^3, respectively. Calculated average depths of penetration within the three above minerals corresponding to different α-particle energies (4.2–8.8 MeV) of the ^{238}U decay series are listed in Table 2. The simulated *SRIM/TRIM* results from the altered zones exhibit average radii with size ranges of 12–19 μm in biotite (4.20–5.49 MeV) and 40–50 μm in plagioclase (7.69–8.79 MeV). These simulated results compare reasonably well with the observed radii of irradiation in biotite (i.e. ~15 μm; Fig. 5*b*) and plagioclase (i.e. ~45 μm; Fig. 5*c*).

Matrix reaction domain

The grain boundaries of plagioclase occasionally preserve some reaction fronts composed of altered phases. These fronts can provide insights into the

TABLE 1. (contd)

	Radio-centre		Unidentified *LREE* phase		Monazite reaction domain				
	13 Urn	14 Urn	15	16	17 Mnz1	18 Mnz1	19 Mnz2	20 Mnz3	21 Mnz3
SiO_2	0.09	0.06	15.43	17.90	0.40	0.28	0.54	0.81	1.16
Al_2O_3	b.d.l	b.d.l	8.68	7.28	0.01	b.d.l	0.04	0.02	0.02
CaO	0.12	b.d.l	2.73	2.73	0.76	0.57	3.27	4.95	5.44
Y_2O_3	0.24	0.14	0.24	0.44	0.97	0.91	1.99	1.99	2.01
La_2O_3	0.02	b.d.l	13.35	12.30	13.71	13.48	10.38	8.38	6.86
Ce_2O_3	b.d.l	b.d.l	27.10	25.20	27.72	28.17	20.60	17.27	14.30
Pr_2O_3	0.42	0.31	2.33	2.40	2.95	3.13	2.26	1.91	1.61
Nd_2O_3	0.04	b.d.l	9.43	10.20	11.56	12.53	8.59	7.43	6.35
SmO	b.d.l	b.d.l	1.72	2.21	2.13	2.66	1.56	1.50	1.43
Gd_2O_3	0.11	b.d.l	0.70	1.20	1.70	2.23	1.53	1.48	1.39
Dy_2O_3	0.04	b.d.l	0.07	0.14	0.41	0.48	0.59	0.74	0.80
Ho_2O_3	b.d.l	b.d.l	0.11	0.17	0.06	b.d.l	0.01	0.30	0.21
UO_2	81.25	77.64	0.11	0.37	0.18	0.10	1.08	1.06	1.03
ThO_2	4.27	5.28	1.81	0.04	4.18	2.12	14.68	20.67	25.36
PbO	12.54	16.35	0.01	0.06	0.31	0.17	1.07	1.21	1.76
P_2O_5	b.d.l	b.d.l	0.10	0.34	29.80	30.40	30.08	27.38	29.08
Total	100.0	100.2	84.9	84.6	97.2	97.6	98.6	97.3	99.3
$\Sigma LREE_2O_3$	0.59	0.31	54.71	53.70	60.20	62.70	45.50	38.71	32.73
Oxygen					4	4	4	4	4
Si					0.016	0.011	0.021	0.033	0.046
Al					0.000	0.000	0.002	0.001	0.001
Ca					0.032	0.024	0.138	0.217	0.230
Y					0.021	0.019	0.042	0.043	0.042
La					0.202	0.197	0.150	0.127	0.100
Ce					0.406	0.408	0.296	0.259	0.206
Pr					0.043	0.045	0.032	0.029	0.023
Nd					0.165	0.177	0.120	0.109	0.089
Sm					0.031	0.038	0.022	0.022	0.020
Gd					0.023	0.029	0.020	0.020	0.018
Dy					0.005	0.006	0.007	0.010	0.010
Ho					0.001	0.000	0.000	0.004	0.003
U					0.002	0.001	0.009	0.010	0.009
Th					0.038	0.019	0.131	0.193	0.228
Pb					0.003	0.002	0.011	0.013	0.019
P					1.009	1.020	1.000	0.950	0.971
(P + Si)					1.025	1.031	1.021	0.983	1.016
(Th + U + Pb + Ca)					0.075	0.046	0.290	0.433	0.485
(M + *HREE* + Y)					0.027	0.025	0.049	0.057	0.055

Mineral abbreviations are after Whitney and Evans (2010); b.d.l: below detection limit, other elements below detection limits are not shown.

replacement mechanism and fluid chemistry, and thus, BSE and X-ray element images (Fig. 7) of a representative reaction domain were obtained. The BSE image reveals high porosity and roughness in plagioclase within the reaction front, as shown by the white dotted circle (Fig. 7*a*), indicating dissolution of the mineral accompanied by mass/volume-loss during replacement. The replacement interface seems to have moved inwards towards the core of the mineral and consequently the domain gained K and became depleted in Na during this process, implying formation of K-feldspar from plagioclase. Furthermore, EPMA within the porous plagioclase (BSE: Fig. 7*a*) shows an increase in

TABLE 2. Penetration depth of the α particle in biotite, chlorite, and plagioclase; comparison between Monte-Carlo simulated and observed values.

	α decay (^{238}U series)	α energy (E_α) in MeV	Monte–Carlo values (μm)	Mean radius of damaged aureoles (present study; μm)
Biotite	$^{238}U \rightarrow {}^{234}U$	4.20	12.7	12–19 (altered halo)
	$^{234}U \rightarrow {}^{230}Th$	4.78	15.3	
	$^{230}Th \rightarrow {}^{226}Ra$	4.69	14.9	
	$^{226}Ra \rightarrow {}^{222}Rn$	4.79	15.3	
	$^{222}Rn \rightarrow {}^{218}Po$	5.49	18.8	
	$^{218}Po \rightarrow {}^{214}Pb$	6.00	21.4	
	$^{214}Po \rightarrow {}^{210}Pb$	7.69	31.4	34–46 (radiohalo)
	$^{210}Po \rightarrow {}^{206}Pb$	5.31	17.8	
	$^{212}Po \rightarrow {}^{208}Pb$	8.79*	38.8	
Chlorite	$^{238}U \rightarrow {}^{234}U$	4.20	15.2	
	$^{234}U \rightarrow {}^{230}Th$	4.78	18.2	
	$^{230}Th \rightarrow {}^{226}Ra$	4.69	18.0	
	$^{226}Ra \rightarrow {}^{222}Rn$	4.79	18.2	
	$^{222}Rn \rightarrow {}^{218}Po$	5.49	22.6	
	$^{218}Po \rightarrow {}^{214}Pb$	6.00	25.4	
	$^{214}Po \rightarrow {}^{210}Pb$	7.69	37.6	34–43 (radiohalo)
	$^{210}Po \rightarrow {}^{206}Pb$	5.31	21.5	
	$^{212}Po \rightarrow {}^{208}Pb$	8.79*	46.3	
Plagioclase	$^{238}U \rightarrow {}^{234}U$	4.20	16.8	
	$^{234}U \rightarrow {}^{230}Th$	4.78	20.2	
	$^{230}Th \rightarrow {}^{226}Ra$	4.69	19.7	
	$^{226}Ra \rightarrow {}^{222}Rn$	4.79	20.3	
	$^{222}Rn \rightarrow {}^{218}Po$	5.49	24.8	
	$^{218}Po \rightarrow {}^{214}Pb$	6.00	28.2	
	$^{214}Po \rightarrow {}^{210}Pb$	7.69	41.2	40–50 (altered halo)
	$^{210}Po \rightarrow {}^{206}Pb$	5.31	23.6	
	$^{212}Po \rightarrow {}^{208}Pb$	8.79*	50.7	

(*) ^{232}Th decay series.

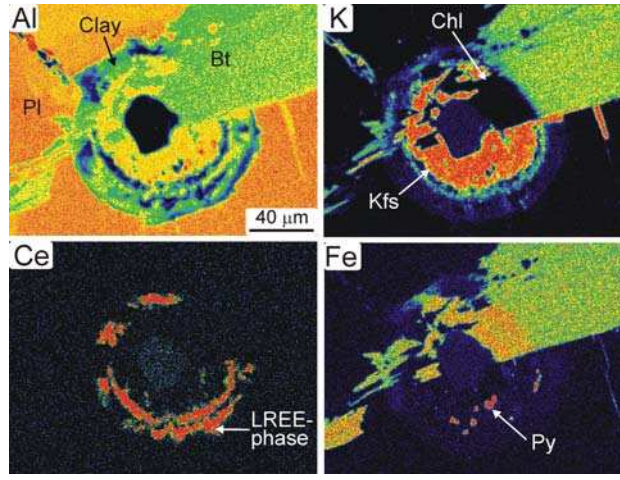


FIG. 6. X-ray elemental maps of Al, K, Ce and Fe from a selected reaction aureole within plagioclase.

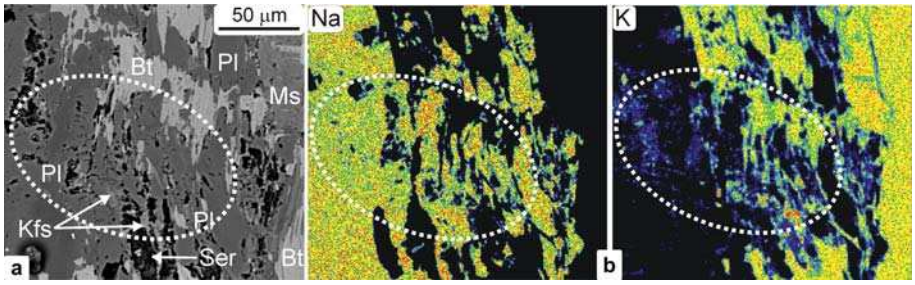


FIG. 7. BSE (*a*) and X-ray element (Na and K) images (*b*) of a selected reaction domain from the matrix, where the white dotted circle represents the reaction front.

X_{Kfs} (~0.14) towards the grain boundaries (analysis 4: Table 1), as complemented by the Na and K elemental distribution maps (Fig. 7*b*). Thus, the micro-textures and the compositional variations (Fig. 7 and analyses 3–5: Table 1), exhibit dissolution-replacement of the pristine phases that advanced along the grain boundaries and the pre-existing cracks inwards into the crystal, resulting in precipitation of K-feldspar at the contact of plagioclase and the subsequent formation of sericite (Fig. 7*a* and analysis 6: Table 1).

Monazite: alteration and element mobility

The *REE*-bearing minerals in the sample studied are monazite, zircon, xenotime, apatite and rarely uraninite, while monazite is volumetrically the most important and abundant *LREE* phase (Fig. 5*a*). Regardless of its high resistance to alteration (Van Emden *et al.*, 1997; Roy, 1999), studies have demonstrated that monazite can suffer partial to complete alteration under moderate temperatures, by reaction with aqueous fluids (Poitrasson *et al.*, 1996, 2000; Rasmussen and Muhling, 2007, 2009). Natural monazites can potentially leach *LREE*s following dissolution in the presence of low temperature, highly saline and oxidizing brines (Mathieu *et al*., 2001). Such dissolution, substantiated by low-temperature solubility experiments on natural monazite (Oelkers and Poitrasson, 2002) or synthetic end-members (Poitrasson *et al*. 2004) determined in the H_2O–NaCl–HCl system, shows enhanced solubility of the mineral in both highly acidic and alkaline solutions. Furthermore, Harlov *et al*. (2011) experimentally demonstrated monazite dissolution is enhanced by alkali-rich fluids, but the solubility decreases with addition of Al. Therefore, understanding the elemental distribution in monazite and its participation during the alteration process is a critical aspect pertaining to its fluid-assisted alteration. For this purpose, BSE and X-ray element (of P, Ca, Th, Y, Ce and La; Fig. 8*a*) images of a representative monazite grain were obtained, coupled with spot EPMA. Monazite shows three distinct zones within the selected domain (Mnz_1 through Mnz_3, Fig. 8*a*). Mnz_1 represents the relict core surrounded by secondary Mnz_2, where the two zones exhibit broadly similar brightness in BSE. These zones are then systematically encircled by a corona of chemically heterogeneous Mnz_3 showing dissolution textures involving an irregular, corroded but sharp, interface with Mnz_1/Mnz_2. The altered zone appears to be pitted and irregular at the interior with a semi-concentric succession of tiny phases, which subsequently got stranded with augmented islands of micrometre-sized phases towards the boundary. X-ray maps (Fig. 8*a*) reveal enrichment in Ca, Th, and Y and depletion in Ce and La in Mnz_2, compared to its core (Mnz_1), where the interface is broadly sharp. Compared to the inner parts (Mnz_1 and Mnz_2), the felt-textured and altered rim (Mnz_3) is characterized by a depletion of major monazite components (Ce and La; Fig. 8*a*), compensated by an enrichment in P, Th, Y and Ca (Fig. 8*a*), similar to that observed by Poitrasson *et al.* (2000). Accurate EPMA could not be performed on Mnz_3 due to the micrometre-scale intergrowth with Th-Y-U-bearing phases. Nevertheless, representative data obtained for Mnz_1 through Mnz_3 show a reverse correlation between $\sum LREE$ and Th + U + Ca + Si + Y from core to rim (Fig. 8*b* and analyses 17–21: Table 1). The stranded islands within Mnz_3 most probably represent phases such as $(Th,U)SiO_4$ (thorite, a low-temperature polymorph of huttonite) and $USiO_4$ (coffinite).

The incorporation of Th and U in Mnz_2/Mnz_3 indicates the brabantite-cheralite substitution $[(Th,U)^{4+} + Ca^{2+} = 2(REE)^{3+}$, Fig. 9*a*] to be the

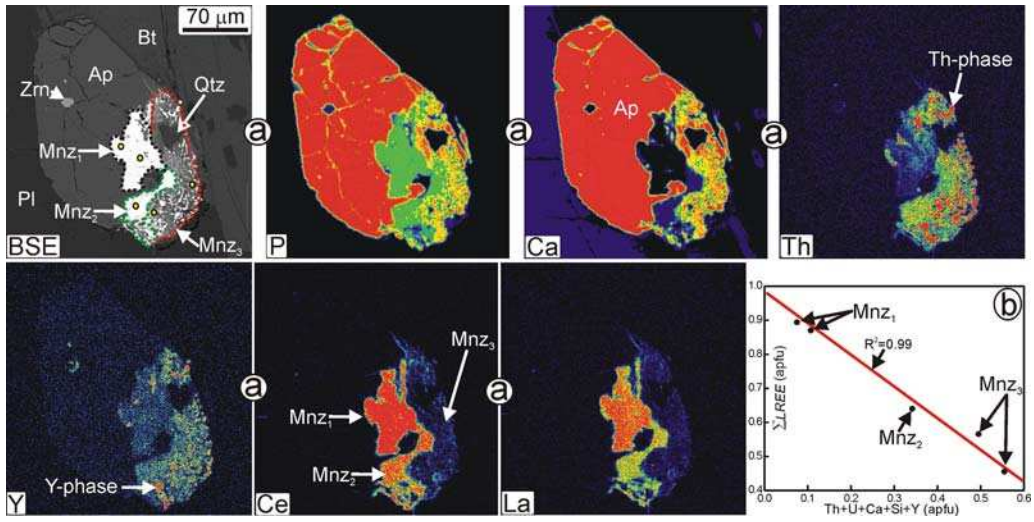


FIG. 8. BSE and X-ray elemental images of P, Ca, Th, Y, Ce and La of a selected monazite grain (*a*), where the yellow circles (in the BSE image) represent EPMA and the dotted lines mark the zone boundaries. Plot of Σ*LREE vs.* Th + U + Ca + Si + Y of the different zones in monazite (Mnz_{1-3}) (*b*).

dominant replacement mechanism. A steady enrichment in Th, U, Y, Ca, Pb, Si and depletion in *LREE*s was observed while moving away from the core (Fig. 9*b*), which is substantiated by the typical *LREE* depletion in the dissolved monazite (Mnz_3), when compared to Mnz_1. The *REE* pattern of Mnz_{1-3} and the *LREE*-phase within the reaction aureoles of plagioclase are comparable (Fig. 9*c*).

Discussion

Alteration halo: inception to replacement

Due to the presence of U and Th in the structure of uraninite (analyses 13–14: Table 1), the mineral possesses radio-nuclei of ^{238}U, ^{235}U and ^{232}Th. Alpha-decay of these radio-nuclei generates different energies of α-particles, and subsequently creates structural defects within the surrounding minerals (e.g. Ewing, 1994). As mentioned before, the outermost diameter of the radiohalo increases linearly with the size of the corresponding uraninite grain (Fig. 3). In addition, a systematic decrease in intensity and broadening of the characteristic Raman bands within the radiohalos of biotite and chlorite were observed (Fig. 4). These features, along with well-preserved aureoles containing secondary phases within biotite and plagioclase (Fig. 6) indicate prolonged irradiation of α particles, which eventually weakened the structure of the host phases around large (≥10 μm) uraninite grains and consequently enhanced the vulnerability of these aureoles to subsequent fluid alteration, resulting in considerable replacement of these metamict areas with secondary compatible phases. The preservation of halos indicates an extended period of time (≥100 Ma; Gentry, 1973, 1974) under near surface 'cold conditions', because thermal annealing can potentially erase these halos at a higher temperature (>150°C, Laney and Laughlin, 1981). Due to the occurrence of secondary phases, the damaged areas within biotite and plagioclase are not radiohalos *sensu stricto.* Rather they represent entirely transformed or replaced micrometre-scale aureoles, filled with secondary phases that formed during low-temperature alteration of the host minerals (e.g. Seydoux-Guillaume *et al.*, 2009; Prochazka *et al.*, 2011) and thus should be better termed here as 'replacement halos'. In addition, chloritization of biotite is restricted invariably to the replacement halos surrounding uraninites (e.g. Fig. 5*b*). As suggested previously by Seydoux-Guillaume *et al.* (2009), these replacement halos represent the starting points of fluid alteration; and accordingly the alteration of biotite to chlorite within the halos in the present study substantially validates the above proposition. On the contrary, the preserved halos within chlorite resemble the radiohalos well, similar to those documented by Pal (2004) and Nasdala *et al.* (2006).

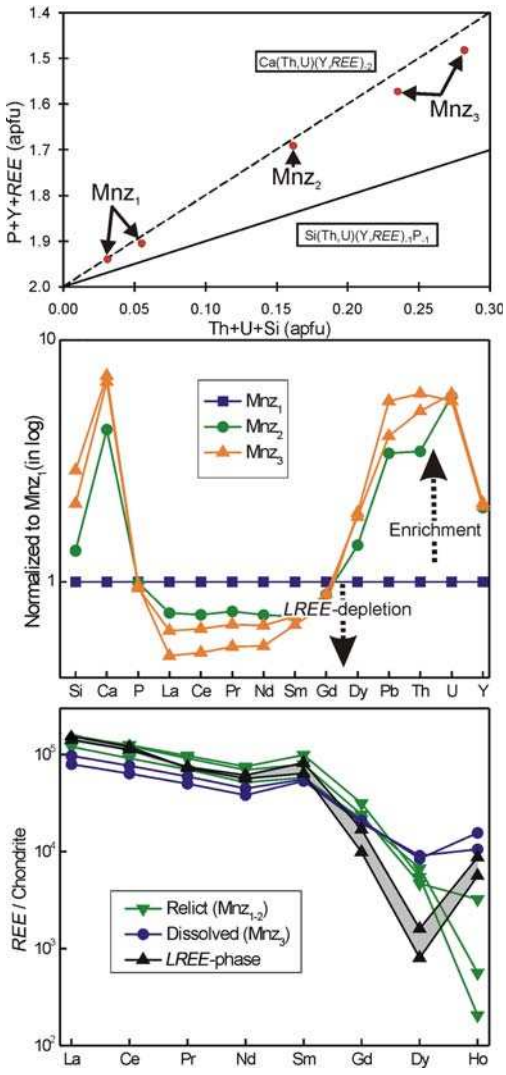


FIG. 9. Plots illustrating the composition of different zones of monazite within the reaction domain, documenting the cheralite-brabantite substitution (*a*); *REE* plots for Mnz_2 and Mnz_3 normalized against Mnz_1 demonstrating the chemical changes associated with alteration (*b*); *REE* patterns (normalized after Taylor and McLennan 1985) of the relict and dissolved monazite (within the monazite reaction domain) and the newly-formed *LREE* phase (within reaction aureoles of plagioclase) (*c*). Shaded area represents *REE* pattern of the *LREE* phase.

Fluid: interaction and pathways

As radiation damage is a post-crystallization process it can potentially create areas which may act subsequently as possible sites for chemical alteration (Seydoux-Guillaume *et al.*, 2009; Prochazka *et al.*, 2011). The systematic distribution of K-feldspar encircling uraninite within the damaged albitic zone (Fig. 6) indicates K-feldspar formation following structural damage in plagioclase. The above inference is in agreement with the replacement of Na-feldspar by K-feldspar in the matrix (Fig. 7), by an influx of a K-rich fluid (reaction 1) that is common during low- to middle-temperature alkali metasomatism (Zhao, 2005).

$$\underset{Ab}{NaAlSi_3O_8} + K^+_{aq} = \underset{Kfs}{KAlSi_3O_8} + Na^+_{aq} \qquad (1)$$

Later, the replacement of K-feldspar by a clay mineral phase (Fig. 6) through argillic alteration represents a superimposed event of acidic alteration associated with K-removal and Fe + Mg addition that is partly accomplished by the modelled reactions 2 and 3.

$$\underset{Kfs}{1.5KAlSi_3O_8} + H^+ = \underset{Mus}{0.5KAl_3Si_3O_{10}(OH)_2} + \underset{Qtz}{3SiO_2} + K^+_{aq} \qquad (2)$$

$$\underset{Mus}{4KAl_3Si_3O_{10}(OH)_2} + \underset{Qtz}{12SiO_2} + 6Mg^{2+}_{aq} + 4H^+ = \underset{Ilt}{3KMg_2Al_4Si_8O_{20}(OH)_4} + K^+_{aq} \qquad (3)$$

Sericitization of K-feldspar in several reaction domains within plagioclase (Fig. 7*a*) further supports acidic alteration. Likewise, biotite aureoles were replaced by chlorite (cf. Prochazka *et al.*, 2011), where the replacement was synchronous with the acidic alteration, which can be explained by the model reaction 4 (cf. Parry and Downey, 1982).

$$\underset{Phl}{2KMg_3AlSi_30_{10}(OH)_2} + 4H^+ = \underset{Clin}{Mg_5Al_2Si_30_{10}(OH)_8} + 2K^+_{aq} + Mg^{2+}_{aq} + \underset{Qtz}{3SiO_2} \qquad (4)$$

The close spatial relationship of the *LREE* phase together with K-feldspar within plagioclase (Fig. 6) implies *LREE* precipitation to be associated with alkali metasomatism. The precipitation of the pyrite along with the *LREE* phase provides evidence for local change in redox or f_{S_2} conditions (Figs 5*i*, 6). Such *LREE*-enrichment, associated with sulfide minerals was reported by various

earlier workers (Rimsaite, 1982; Wood and William-Jones, 1994). The uneven distribution of sericite in the matrix and the rare occurrence of the mineral within the damaged domain suggest micrometre-scale variation in the fluid/rock ratio. As a result, the rock studied witnessed sequential infiltration of multi-component aqueous fluid (K-*LREE*s-Fe-S), where the replacement took place at low temperature (≤150°C).

The occurrence of reaction aureoles was not only restricted to grain boundaries, where easy access of the fluid phase occurred; rather they are equally abundant in the intra-granular domains surrounding the uraninite grains (Fig. 5*a*). The secondary phases within the altered aureoles in biotite and plagioclase could not have formed without the transport of the elements (Fe, Al, Si and K) in a relatively large volume. Therefore, these changes indicate well-connected pathways prevailed at the time of fluid infiltration, which subsequently affected these halos. The association of reaction domains along the grain boundaries (Figs 5*a*, 7) indicate the primary pathways for fluid infiltration. Furthermore, the ubiquitous association of cleavages/fractures in/along the vicinity of the secondary phases within biotite (Figs 5*b*, *e*), and the presence of radial cracks (due to volume expansion, Lee and Tromp, 1995; Seydoux-Guillaume *et al*., 2007; Prochazka *et al.*, 2011; Montel and Giot, 2013; Seydoux-Guillaume *et al*., 2015) around plagioclase (Figs 5*a*, *f*) provided the possible secondary pathways for fluid migration responsible for alteration of the halos within these minerals.

Replacement mechanisms

Solid-state diffusion and fluid-induced replacement are the two processes that mostly explain element transport during metamorphic/metasomatic replacement reactions (e.g. Fisher and Lasaga, 1981; Ashworth and Sheplev, 1997). Diffused compositional boundaries are expected in solid-state diffusion due to inherent chemical potential gradients. On the contrary, fluid-assisted reactions occur due to coupled dissolution-reprecipitation processes driven by a solubility difference between the primary and the replacement phases (Harlov *et al.*, 2005, 2011; Upadhyay and Pruseth, 2012). Catalysis due to the pervasive fluid, results in either a new composition of the same phase or the formation of entirely new phases (Putnis, 2002, 2009; Putnis and Austrheim, 2010). Therefore, the process requires well-connected channels/pathways between the fluid and the reaction front, to facilitate rapid mass transfer between the solids.

Back-scatter electron and X-ray images (Figs 6, 7) along with EPMA (Table 1) show a sharp replacement interface, where the domains gained K and lost Na during the process. Figure 7 exhibits inwards movement of the replacement front, where pore spaces in plagioclase indicate dissolution of the mineral. These reaction textures indicate the insignificant role of solid-state diffusion and consequently, dissolution-reprecipitation is inferred to be the possible process involved in alteration. Numerous experimental studies have been undertaken in the recent past (e.g. Labotka *et al.*, 2004; Niedermeier *et al.*, 2009 and references therein), which provide insights into these processes on a laboratory scale and can be extrapolated to natural conditions. Moreover, the observed textural features in the matrix domain (Fig. 7) are consistent with the results of the experimental work by Niedermeier *et al.* (2009), which is essentially an interface-coupled dissolution-reprecipitation process.

LREE mobilization

The ubiquitous occurrence of the *LREE* phase within the reaction aureoles (Fig. 6) and absence of the same in the vicinity of monazite in the sample (Figs 5*a*, 8*a*) needs to be explained, as these indicate micrometre-scale removal, transportation, and precipitation of the *LREE*s in the sample. The dissolution texture involving monazite (Fig. 8*a*) shows partial replacement of the original monazite by fluid-assisted alteration. Further, the observed brabantite-cheralite substitution mechanism (Fig. 9*a*); depletion of *LREE*s and addition of U, Th, Y and Ca (Figs 8*b*, 9*b*); and the invariable absence of other *LREE*-bearing phases in the vicinity of the dissolved monazite implies extensive leaching of the *LREE*s from the mineral by a hydrothermal fluid. Micro-porosity and a well-connected network between the folia within Mnz_3 (Fig. 8*a*), possibly represent the relict pathways of fluid migration, which enhanced the dissolution process. Similarity in the *REE* patterns of the relict monazite (Mnz_1) and the *LREE* phase within the altered aureoles (Figs 5*c*, *i*) supports chemical evidence for the latter to be the final reaction product of monazite (Fig. 9*c*). Although, the composition of the fluid responsible for dissolution of monazite is ambiguous, the presence of an alkali-enriched, low-temperature fluid is

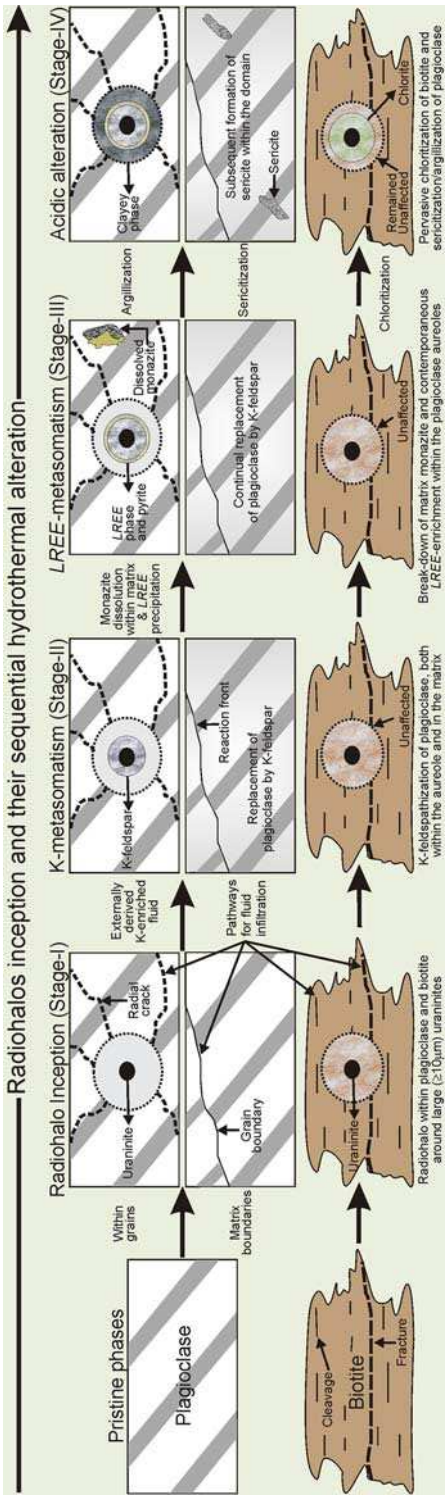


FIG. 10. Schematic representation of the evolutionary sequence of the radiohalo formation (within plagioclase and biotite) and corresponding changes during the subsequent stages of hydrothermal alteration.

most probable, which was responsible for the mobilization of the *LREE*s from the mineral. This inference is further supported by the close spatial relationship between the virgin *LREE* phase and K-feldspar within the reaction aureoles in plagioclase (Fig. 6). Accordingly, the sample exhibits micrometre-scale *LREE* mobilization (see Fig. 5*a*), in which the matrix monazite and plagioclase-hosted aureoles, respectively, acted as the source and the site for *LREE* migration.

Conclusions

Based on the observed geochemical characteristics of the radiohalos and associated alteration-replacement textures, the scenario for the initial formation of the radiohalos and their chronological hydrothermal evolution can be shown using the following proposed sequence as depicted in Fig. 10. (1) Occurrence of intensely damaged radiohalos at the interface between large uraninite grains (≥10 μm) and adjacent biotite and plagioclase hosts indicates that metamictization prevailed in the rock for an extended time period under low temperature (≤150°C) conditions following the initial crystallization of the host minerals (stage-I, Fig. 10). (2) Simultaneous precipitation of K-feldspar within the damaged aureole (Figs 5*a*, 6) and at the grain boundary (Figs 5*a*, 7) of plagioclase points to an influx of a K-rich hydrothermal fluid. The fluid infiltration was facilitated by the grain boundaries and the intragranular radial cracks, leading to local K-metasomatism, i.e. the first replacement event (stage-II, Fig. 10). (3) Stage-III (Fig. 10) accounts for the breakdown of monazite in the matrix and as a consequence coeval formation of the *LREE*-phase within the damaged aureoles in plagioclase, aided and abetted by local variation in the redox conditions or f_{S_2}, as evidenced by the association of pyrite. (4) Late-stage acidic alteration (stage-IV, Fig. 10) was responsible for the formation of a clay mineral (Fig. 6), sericitization of plagioclase (Fig. 7*a*) and chloritization of biotite (Figs 5*b*, 6) around the damaged aureoles, which involved K removal and Fe + Mg addition.

This study clearly shows that micro-aureoles of intense irradiation are suitable structural and chemical traps, where mineral reactions take place.

Acknowledgements

This research work was funded by the Board of Research in Nuclear Science (BRNS), India, Project No. 2011/36/33-BRNS. MKO thanks BRNS and IIT Kharagpur for financial assistance in the form of research fellowships. The authors acknowledge Dipak Chandra Pal for many stimulating discussions. SEM-BSE images and EPMA data were generated by the equipment procured through DST funding (IR/S4/ESF-08/2005) to the Department of Geology and Geophysics, IIT Kharagpur. Saptarshi Sinha is thanked for help with EPMA. Comments by three journal reviewers, along with editorial suggestions by Craig Storey, Peter Williams and Roger Mitchell helped to revise the paper.

References

Ashworth, J.R. and Sheplev, V.S. (1997) Diffusion modelling of metamorphic layered coronas with stability criterion and consideration of affinity. *Geochimica et Cosmochimica Acta*, **61**, 3671–3689.

Bhowmik, S.K., Bernhardt, H.J. and Dasgupta, S. (2010) Grenvillian age high-pressure upper amphibolite-granulite metamorphism in the Aravalli-Delhi Mobile Belt, Northwestern India: New evidence from monazite chemical age and its implication. *Precambrian Research*, **78**, 168–184.

Buick, I.S., Allen, C., Pandit, M., Rubatto, D. and Hermann, J. (2006) The Proterozoic magmatic and metamorphic history of the Banded Gneiss Complex, central Rajasthan, India: LA-ICP-MS U–Pb zircon constraints. *Precambrian Research*, **151**, 119–142.

Buick, I.S., Clark, C., Rubatto, D., Hermann, J., Pandit, M.K. and Hand, M. (2010) Constraints on the Proterozoic evolution of the Aravalli-Delhi Orogenic belt (NW India) from monazite geochronology and mineral trace element geochemistry. *Lithos*, **120**, 511–528.

Ewing, R.C. (1994) The metamict state: 1993 – the centennial. *Nuclear Instruments and Methods in Physics Research*, **B91**, 22–29.

Ewing, R.C., Meldrum, A., Wang, L.M. and Wang, S. (2000) Radiation-induced amorphization. Pp. 319–362 in: *Transformation Processes in Minerals* (S.A.T. Redfern and M.A. Carpenter, editors). Reviews in Mineralogy & Geochemistry, **39**. Mineralogical Society of America and the Geochemical Society, Chantilly, Virginia, USA.

Ewing, R.C., Meldrum, A., Wang, L.M., Weber, W.J. and Corrales, L.R. (2003) Radiation damage in zircon. Pp. 387–425 in: *Zircon* (J.M. Hanchar and P.W.O. Hoskin, editors). Reviews in Mineralogy & Geochemistry, **53**. Mineralogical Society of America and the Geochemical Society, Chantilly, Virginia, USA.

Farges, F. and Calas, G. (1991) Structural analysis of radiation damage in zircon and thorite: An X-ray absorption spectroscopic study. *American Mineralogist*, **76**, 60–73.

Fisher, G.W. and Lasaga, A.C. (1981) Irreversible thermodynamics in petrology. Pp. 171–207 in: *Kinetics of Geochemical Processes* (A.C. Lasaga and R.J. Kirkpatrick, editors). Reviews in Mineralogy & Geochemistry, **8**. Mineralogical Society of America, Washington, USA.

Gentry, R.V. (1973) Radioactive halos. *Annual Review in Nuclear Science*, **23**, 347–362.

Gentry, R.V. (1974) Radiohalos in a radiochronological and cosmological perspective. *Science*, **184**, 62–66.

Gupta, S.N., Arora, Y.K., Mathur, R.K., Iqbaluddin, Prasad, B., Sahai, T.N. and Sharma, S.B. (1997) The Precambrian geology of the Aravalli region, southern Rajasthan and north-eastern Gujarat. *Memoirs of the Geological Survey of India*, **123**, 262.

Harlov, D.E., Wirth, R. and Forster, H.J. (2005) An experimental study of dissolution–reprecipitation in fluorapatite: fluid infiltration and the formation of monazite. *Contributions to Mineralogy and Petrology*, **150**, 268–286.

Harlov, D.E., Wirth, R., and Hetherington, C.J. (2011) Fluid-mediated partial alteration in monazite: the role of coupled dissolution–reprecipitation in element redistribution and mass transfer. *Contributions to Mineralogy and Petrology*, **162**, 329–348.

Hazarika, P., Mishra, B. and Pruseth, K.L. (2015) Diverse tourmaline compositions from orogenic gold deposits in the Hutti-Maski Greenstone Belt, India: Implications for sources of ore-forming fluids. *Economic Geology*, **110**, 337–353.

Heron, A.M. (1953) The Geology of Central Rajputana. *Memoirs of the Geological Survey of India*, **79**, 389 pp.

Janeczek, J. and Eby, R.K. (1993) Annealing of radiation damage in allanite and gadolinite. *Physics and Chemistry of Minerals*, **19**, 343–356.

Joly, J. (1907) Pleochroic halos. *Philosophical Magazine*, **13**, 381–383.

Labotka, T.C., Cole, D.R., Fayek, M., Riciputi, L.R. and Stadermann, F.J. (2004) Coupled cation and oxygen-isotope exchange between alkali feldspar and aqueous chloride solution. *American Mineralogist*, **89**, 1822–1825.

Laney, R. and Laughlin, A.W. (1981) Natural annealing of pleochroic haloes in biotite samples from deep drill holes, Fenton Hill, New Mexico. *Geophysical Research Letters*, **8**, 501–504.

Lee, J.K. and Tromp, J. (1995) Self-induced fracture generation in zircon. *Journal of Geophysical Research*, **100**(B9), 17753–17770.

Mathieu, R., Zetterström, L., Cuney, M., Gauthier-Lafaye, F. and Hidaka, H. (2001) Alteration of monazite and zircon and lead migration as geochemical tracers of fluid paleocirculations around the Oklo–Okélobondo and

Bangombé natural nuclear reaction zones (Franceville basin, Gabon). *Chemical Geology*, **171**, 147–171.

Montel, J.M., and Giot, R. (2013) Fracturing around radioactive minerals: elastic model and applications. *Physics and Chemistry of Minerals*, **40**, 635–645.

Nasdala, L., Wenzel, M., Andrut, M., Wirth, R. and Blaum, P. (2001) The nature of radiohaloes in biotite: experimental studies and modeling. *American Mineralogist*, **86**, 498–512.

Nasdala, L., Wildner, M., Wirth, R., Groschopf, N., Pal, D.C. and Möller, A. (2006) Alpha particle haloes in chlorite and cordierite. *Mineralogy and Petrology*, **86**, 1–27.

Niedermeier, D.R.D., Putnis, A., Geisler, T., Golla-Schindler, U. and Putnis, C.V. (2009) The mechanism of cation and oxygen isotope exchange in alkali feldspars under hydrothermal conditions. *Contributions to Mineralogy and Petrology*, **157**, 65–76.

Oelkers, E.H. and Poitrasson, F. (2002) An experimental study of the dissolution stoichiometry and rates of a natural monazite as a function of temperature from 50 to 230°C and pH from 1.5 to 10. *Chemical Geology*, **191**, 73–87.

Ozha, M.K., Mishra, B., Hazarika, P., Jeyagopal, A.V. and Yadav, G.S. (2016) EPMA monazite geochronology of the basement and supracrustal rocks within the Pur-Banera basin, Rajasthan: Evidence of Columbia breakup in Northwestern India. *Journal of Asian Earth Sciences*, **117**, 284–303.

Pal, D.C. (2004) Concentric rings of radioactive halo in chlorite, Turamdih uranium deposit, Singhbhum Shear Zone, Eastern India: a possible result of ^{238}U chain decay. *Current Science*, **87**, 662–667.

Parry, W.T. and Downey, L.M. (1982) Geochemistry of hydrothermal chlorite replacing igneous biotite. *Clays and Clay Minerals*, **30**, 81–90.

Poitrasson, F., Chenery, S. and Bland, D.J. (1996) Contrasted monazite hydrothermal alteration mechanisms and their geochemical implications for the U–Th–Pb geochronology and nuclear ceramics. *Earth and Planetary Science Letters*, **145**, 79–96.

Poitrasson, F., Chenery, S. and Shepherd, T.J. (2000) Electron microprobe and LA-ICP-MS study of monazite hydrothermal alteration: implications for the U-Th-Pb geochronology and nuclear ceramics. *Geochimica et Cosmochimica Acta*, **64**, 3283–3297.

Poitrasson, F., Oelkers, E., Schott, J. and Montel, J.M. (2004) Experimental determination of synthetic $NdPO_4$ monazite end-member solubility in water from 21°C to 300°C: implications for rare earth element mobility in crustal fluids. *Geochimica et Cosmochimica Acta*, **68**, 2207–2221.

Pouchou, J.L. and Pichoir, F. (1984) A new model for quantitative X-ray microanalyses, Part I: Application to the analyses of homogenous samples. *Recherche Aerospatiale*, **3**, 13–36.

Procházka, V., Seydoux-Guillaume, A.M., Trojek, T., Goliáš, V., Korbelová, Z., Matějka, D. and Novotná, P. (2011) Alteration halos around radioactive minerals in plutonic and metamorphic rocks of the northern Moldanubian area, Bohemian massif. *European Journal of Mineralogy*, **23**, 551–566.

Putnis, A. (2002) Mineral replacement reactions: from macroscopic observations to microscopic mechanisms. *Mineralogical Magazine*, **66**, 689–708.

Putnis, A. (2009) Mineral replacement reactions. Pp. 87–124 in: *Thermodynamics and Kinetics of Water–Rock Interaction* (E.H. Oelkers and Schott, editors). Reviews in Mineralogy & Geochemistry, **70**. Mineralogical Society of America and the Geochemical Society, Chantilly, Virginia, USA.

Putnis, A. and Austrheim, H. (2010) Fluid-induced processes: metasomatism and metamorphism. *Geofluids*, **10**, 254–269.

Rasmussen, B. and Muhling, J.R. (2007) Monazite begets monazite: evidence for the dissolution of detrital monazite and reprecipitation of syntectonic monazite during low-grade regional metamorphism. *Contributions to Mineralogy and Petrology*, **154**, 675–689.

Rasmussen, B. and Muhling, J.R. (2009) Reactions destroying detrital monazite in greenschist-facies sandstones from the Witwatersrand basin, South Africa. *Chemical Geology*, **264**, 311–327.

Rimsaite, J. (1982) Alteration of radioactive minerals in granite. Pp. 269–280 in: *Ore genesis – the state of the art* (G. C. Amstutz, editor). Springer, Berlin.

Roy, P.S. (1999) Heavy mineral beach placers in Southeastern Australia: their nature and genesis. *Economic Geology*, **94**, 567–588.

Seydoux-Guillaume, A.M., Wirth, R. and Ingrin, J. (2007) Contrasting response of $ThSiO_4$ and monazite to natural irradiation. *European Journal of Mineralogy*, **19**, 7–14.

Seydoux-Guillaume, A.M., Montel, J.M., Wirth, R. and Moine, B. (2009) Radiation damages in diopside and calcite crystals from uranothorianite inclusions. *Chemical Geology*, **261**, 318–332.

Seydoux-Guillaume, A.M., Montel, J.M., Bingen, B., Bosse, V., De Parseval, P., Paquette, J.L. and Wirth, R. (2012) Low-temperature alteration of monazite: Fluid mediated coupled dissolution-precipitation, irradiation damage, and disturbance of the U-Pb and Th-Pb chronometers. *Chemical Geology*, **330**, 140–158.

Seydoux-Guillaume, A.M., Bingen, B., Paquette, J.L. and Bosse, V. (2015) Nanoscale evidence for uranium mobility in zircon and the discordance of U–Pb chronometers. *Earth and Planetary Science Letters*, **409**, 43–48.

Taylor, S.R. and McLennan, S.M. (1985) *The Continental Crust: Its Composition and Evolution.* Blackwell, Oxford, UK, 312 pp.

Upadhyay, D. and Pruseth, K.L. (2012) Fluid-induced dissolution breakdown of monazite from Tso Morari complex, NW Himalayas: evidence for immobility of trace elements. *Contributions to Mineralogy and Petrology*, **164**, 303–316.

Van Emden, B., Graham, J. and Lincoln, F.G. (1997) The incorporation of actinides in monazite and xenotime from placer deposits in western Australia. *The Canadian Mineralogist*, **35**, 95–104.

Whitney, D.L. and Evans, B.W. (2010) Abbreviations for names of rock-forming minerals. *American Mineralogist*, **95**, 185–000.

Wood, S.A. and Williams-Jones, A.E. (1994) The aqueous geochemistry of the rare-earth elements and yttrium 4. Monazite solubility and REE mobility in exhalative massive sulfide-depositing environments. *Chemical Geology*, **115**, 47–60.

Weber, W.J., Ewing, R.C., Catlow, C.R.A., De La Rubia, T. D., Hobbs, L.W., Kinoshita, C. and Zinkle, S.J. (1998) Radiation effects in crystalline ceramics for the immobilization of high-level nuclear waste and plutonium. *Journal of Materials Research*, **13**, 1434–1484.

Ziegler, J.F., Biersack, J.P. and Littmark, U. (2006) SRIM 2006. Available from http://srim.org/

Zhao, F. (2005) *Alkali-metasomatism and uranium mineralization.* Pp. 343–346 in: *Mineral Deposit Research (Meeting the Global Challenge).* Springer, Berlin.